separations

MDPI

Article

Design Methodology for a Low-Shear Rotating Swirler

Zheng Si [1,2], Yipeng Ji [1,2,*], Jiaqing Chen [1,2], Xiujun Wang [3,*], Hong Du [3], Jian Zhang [3], Hai Yu [1,2], Qiang Ren [1,2] and Zhao Hua [2]

[1] Beijing Institute of Petrochemical Technology, Beijing 102617, China; jiaqing@bipt.edu.cn (J.C.)
[2] Beijing Key Laboratory of Pipeline Critical Technology and Equipment for Deepwater Oil & Gas Development, Beijing 102617, China
[3] CNOOC Research Institute Co., Ltd., Beijing 100028, China
* Correspondence: jiyipeng@bipt.edu.cn (Y.J.); wangxj89@cnooc.com.cn (X.W.)

Abstract: The tubular dynamic hydrocyclone (TDH) holds great potential for the pre-deoiling of offshore oil platforms. However, the shear and turbulence in the flow field can cause the oil droplets, the dispersed phase in water, to break up when the swirling flow is produced by the swirler. A design method is proposed for the low-shear rotary swirler (LSRS) of TDH, the aim of which is to reduce the shear force and local turbulence during the fluid forming swirling flow. The blade setting angle of the LSRS is calculated based on the relative velocity vector between the fluid and the swirler. The distribution characteristics of the tangential velocity and turbulence in the TDH with LSRS are simulated by Computational Fluid Dynamics (CFD). The maximum stable droplet diameter is analyzed. The results show that the shear stress and turbulence energy dissipation rates are reduced by 74.6% and 68.5%, respectively, and that the stable droplet diameter is increased by more than 60%, compared to the conventional rotating swirler. In addition, a TDH prototype with LSRS was tested in an offshore oil field by continuous operation for more than 36 h. The average separation efficiency was 83%, and the average underflow oil concentration was 27 mg/L. The research also found that the drastic changes in the tangential velocity along the axial direction were critical to shear. Moreover, the results make up for the deficiency of the spatial variation of the tangential velocity in the dynamic cyclone separator.

Keywords: tubular dynamic hydrocyclone; oil–water separation; low shear; design model; field experiments

Citation: Si, Z.; Ji, Y.; Chen, J.; Wang, X.; Du, H.; Zhang, J.; Yu, H.; Ren, Q.; Hua, Z. Design Methodology for a Low-Shear Rotating Swirler. *Separations* **2023**, *10*, 550. https://doi.org/10.3390/separations10110550

Academic Editor: Chaolang Chen

Received: 1 October 2023
Revised: 26 October 2023
Accepted: 26 October 2023
Published: 28 October 2023

1. Introduction

Tubular hydrocyclones use centrifugal force to achieve rapid liquid–liquid separation, and are low cost and space saving compared to conventional vessel type separators [1]. However, the high shear and turbulence caused by the drastic changes in tangential velocity break up the large droplets of the disperse phase. According to Stokes' law, a negative relationship exists between the mean diameter of the dispersed phase and the separation efficiency of the hydrocyclone [2,3].

The conventional static hydrocyclone induces a swirling flow by the tangential inlet, and the oil droplets with a diameter larger than 60 μm are broken [4,5]. The smaller droplet size (<40 μm) produced after broken is insensitive to centrifugal force, resulting in lower separation efficiency [4,5]. The deformation and breakage of oil droplets during the formation of the swirling flow induced by static guide vanes also has been observed in axial inlet hydrocyclones by Liu et al. [6,7].

In order to reduce the oil droplet breakage induced by shear and turbulence during the formation swirling flow, including the involute line feed body [8], the vane angle of the swirler [9,10], the overflow structure [11], the type and size of the separator barrel [12], and so on, have been studied. Among them, the swirler structure is the main factor influencing the variation of tangential velocity [13]. The compressor blade design method

has been used to obtain a low-shear guide vane of a static axial inlet hydrocyclone [14,15]. A hydrocyclone coalescer (HCC) has also been developed in which the swirler is designed as a spiral cascade to promote the coalescence of dispersed oil droplets [16,17].

The dynamic hydrocyclone uses a motor to drive a rotating drum, and the fluid forms a swirling flow directly driven by the drum. Unlike the static hydrocyclone, the dynamic hydrocyclone does not require a booster pump; moreover, it also has a higher separation efficiency and is more robust [17,18]. Several studies have proposed the novel Tubular Dynamic Hydrocyclone (TDH) with a static barrel and straight impeller blades to induce the swirling flow [19,20]. Rotating blade structures, which have been found to affect the separation efficiency of TDH, were investigated in a recent study, and the backward curved blade performed better in the separation process than the straight blade [21]. The Voraxial Impeller Induced Cyclonics developed by Enviro Voraxial Technology uses a hollow spiral impeller blade to reduce the shear stress as the fluid begins to rotate [22–24].

The Beijing Institute of Petrochemical Technology has conducted a series of studies on dynamic hydrocyclone technology since 2007, and the high shear stress and turbulence were generated when the fluid was induced by the rotational swirler, and the separation efficiency at a high rotational speed does not achieve the expected results. The study by Perissinotto et al. on droplet deformation and the fragmentation of dispersed phase droplets in centrifugal pumps showed that a high turbulence intensity existed in the front of the centrifugal pump inlet, so that the dispersed droplets are broken before entering the pump chamber [25–28].

Therefore, reducing the peak value of the local shear stress and turbulence intensity without changing the centrifugal field strength is crucial to improve the separation efficiency of tubular hydrocyclones, especially when using polymer flooding on offshore oil fields, where the dispersed oil phase is relatively easy to emulsify [29,30]. The concept of the low-shear rotating swirler (LSRS) for dynamic hydrocyclone has been proposed, however, no design method for LSRS was developed until now. In order to reveal the shear mechanism in the swirl flow forming process of dynamic hydrocyclones, the cylindrical swirl is expanded and simplified to two-dimensional flow while the radial velocity and fluid inertia effect were ignored. In addition, the changes in the tangential velocity along the axial and radial directions were analyzed by computational fluid dynamics (CFD). According to the shear mechanism, the LSRS design methodology for TDH was proposed, which helps prevent the oil droplets from breaking up before being isolated. The variation of shear stress and the turbulence energy dissipation rate with the swirler blade setting angle was also analyzed using CFD. The separation performance of the TDH with the LSRS was tested in an offshore oil field.

2. Design Model for the LSRS

2.1. Structure of the TDH

The structure of the TDH, including the axial inlet, swirler, vortex enhancement cone, static separation barrel, vortex controller, underflow, and overflow, is shown in Figure 1. The separated oil is discharged in the reverse direction of the continuous flow, and a vortex controller that is coaxial with the static separation barrel is installed upstream of the underflow.

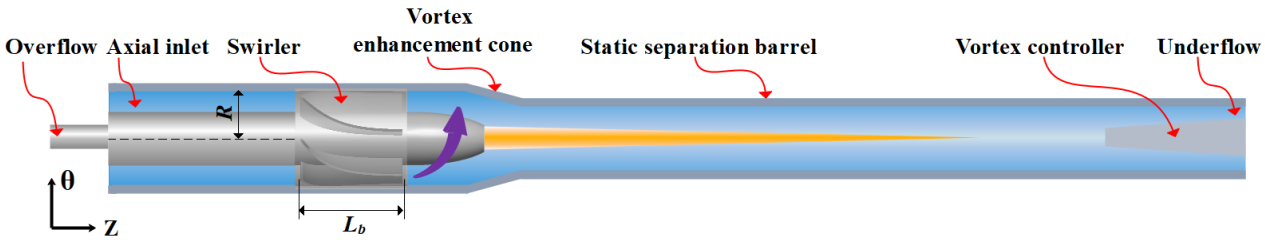

Figure 1. Structure of the TDH.

Raw water enters the TDH via the axial inlet and is then swirled by the swirler. The centrifugal force is then increased by the vortex enhance cone, before the fluid flow into the static separation barrel. In the static separation barrel, the strong centrifugal force takes the high-density water migrated towards the wall of the barrel and discharged through the underflow. The low-density oil converges to the center of the static separation barrel and forms oil core, which is discharged through the overflow.

2.2. Low-Shear Rotating Swirler (LSRS)

The rotating swirler is a key component of the TDH and its structure and direction of rotation are shown in Figure 2a. Assume that the fluid flows on a cylindrical surface centered on the axis of rotation. A cylindrical coordinate system is built in Figure 2b, the coordinates (0, 0) of which are on the axial line of the swirler and 10 mm away from the entrance side of the blade, and the z axial points to the export side. The swirler is set as the reference system. Then, the relative tangential velocity between the fluid and the swirling blade for any cylindrical surface is given by

$$\overrightarrow{V'_{\mathrm{in}-\theta}} = -\vec{\omega} R_{\mathrm{i}} \tag{1}$$

where R_{i} is the radius of the cylindrical flow surface, and its unit is the meter, and $\vec{\omega}$ is the angular velocity of the swirler in rad/s.

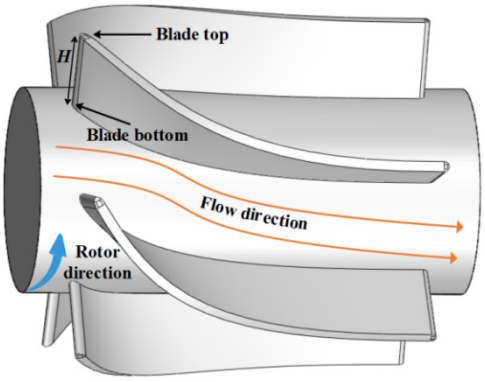

(**a**) Swirler structure.

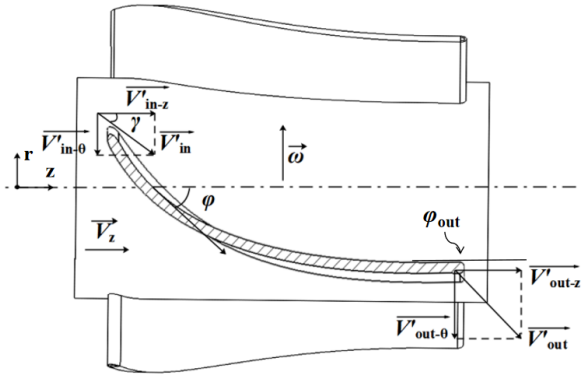

(**b**) Relative velocity between the fluid and swirler blade.

Figure 2. Diagram of TDH swirler.

Assuming a constant velocity of the incoming axial $\overrightarrow{V'_{\mathrm{in}-z}}$, the relative axial velocity of the $\vec{V_z}$ with regard to the swirler at the inlet section of the swirler is

$$\overrightarrow{V'_{\mathrm{in}-z}} = \vec{V_z} = \frac{Q_{\mathrm{in}}}{A_{\mathrm{in}}} \tag{2}$$

where A_{in} is the cross-sectional area at the inlet of the swirler in m^2, and Q_{in} is the feed flow rate in m^3/s.

2.2.1. Inlet Setting Angle of Swirler Blade

The relative velocity vector of the fluid at the inlet section of the swirler can be regarded as the sum of $\vec{V'}_{in-z}$ and $\vec{V'}_{in-\theta}$:

$$\overrightarrow{V'_{in}} = \overrightarrow{V'_{in-\theta}} + \overrightarrow{V'_{in-z}} \tag{3}$$

As shown in Figure 2b, the fluid incidence angle γ is the angle between the relative velocity and the axis of rotation, and the setting angle φ is the angle between the tangent line of the blade surface and the axis of rotation. In the case of straight impeller blades, the inlet setting angle φ_{in} is zero and the fluid will directly impact on the side wall of the swirler. As a result, the fluid is intensely sheared at the inlet of the swirler. When $\gamma = \varphi_{in}$, the direction of the relative velocity is parallel to the swirler blade, the shear caused by the change of tangential velocity in the axial direction can be eliminated, and a low-shear swirling process can be achieved. Based on the velocity vector, the inlet setting angle of the low-shear swirler blade can be expressed as follows

$$\varphi_{in} = \gamma = \arctan\frac{\vec{V}_z}{\overrightarrow{V'_{in-\theta}}} \tag{4}$$

2.2.2. Outlet Setting Angle of Swirler Blade

The relative velocity between the fluid and the blade at the swirler outlet cross-section is

$$\overrightarrow{V'_{out}} = \overrightarrow{V'_{out-\theta}} + \overrightarrow{V'_{out-z}} \tag{5}$$

$$\overrightarrow{V'_{out-z}} = \frac{\vec{V}_z}{\cos\varphi_{out}} \tag{6}$$

Here, $\vec{V'}_{out-\theta}$ is the relative tangential velocity in the outlet section of the swirler in m/s, $\vec{V'}_{out-z}$ is the relative velocity at the outlet section of the swirler in m/s, and φ_{out} is the outlet setting angle of the swirler blade.

Ignoring the blade's thickness and assuming that the number of swirler blades is infinite, then the fluid would be stationary relative to the swirler in the direction of the rotation at the swirler outlet section when φ_{out} is 0°. Thus,

$$\overrightarrow{V'_{out-\theta}} = 0 \tag{7}$$

2.2.3. Design Parameters

According to Equation (2), when the angular velocity and flow rate Q_{in} are constant, $\overrightarrow{V'_{in-\theta}}$ increases linearly with R_i, and $\vec{V}_z$ remains the same. To ensure that $\gamma = \varphi_{in}$, the inlet setting angle must be a variable in the dimension of the swirler blade height. The design parameters of the proposed TDH with the LSRS are shown in Table 1. The outlet setting angle φ_{out} was set to a constant value of 0°.

Table 1. Design parameters of the TDH with the LSRS.

Design Parameters	Value
Design capacity (Q_{in})	5.0 m^3/h
Blade height (H)	15.0 mm
Angular velocity (ω)	146.6 rad/s
Number of blades	6
Swirler radius (R)	35.0 mm
Blade length (L_b)	70.0 mm

3. Flow Field Characteristics Analyzed by Numerical Simulation

3.1. Numerical Simulation Model

3.1.1. Model Description

Among the various turbulence models, the Reynolds Stress Model (RSM) and the Large Eddy Simulation (LES) model predict the anisotropic eddy fields accurately [31]. However, compared with LES, the RSM requires less computational effort; therefore, the RSM model was chosen for the numerical simulation of the turbulence model in this study. The continuity equation of the Reynolds Stress Model is as follows:

$$\frac{\partial \rho}{\partial t} + \frac{\partial (\rho u_i)}{\partial x_i} = 0 \tag{8}$$

where $u_i = \overline{u_i} + u_i'$.

The equation of momentum is

$$\frac{\partial}{\partial t}(\rho u_i) + \frac{\partial}{\partial x_j}(\rho u_j u_i) = -\frac{\partial p}{\partial x_i} - \frac{\partial}{\partial x_j}\left(\rho \overline{u_i' u_j'}\right) + \frac{\partial}{\partial x_j}\left[\mu\left(\frac{\partial u_i}{\partial x_j} + \frac{\partial u_j}{\partial x_i}\right)\right] + \rho g_j \tag{9}$$

The RSM transport equation is

$$\frac{\partial}{\partial t}\left(\rho \overline{u_i' u_j'}\right) + \frac{\partial}{\partial x_k}\left(\rho u_k \overline{u_i' u_j'}\right) = D_{ij} + P_{ij} + \Pi_{ij} + \varepsilon_{ij} + S_{ij} \tag{10}$$

The turbulence dissipation term is

$$D_{ij} = -\frac{\partial}{\partial x_k}\left[\rho \overline{u_i' u_j' u_k'} + \overline{p' u_j'}\delta_{ik} + \overline{p' u_i'}\delta_{jk} - \mu\left(\frac{\partial}{\partial x_k}\overline{u_i' u_j'}\right)\right] \tag{11}$$

The stress diffusion term is

$$P_{ij} = -\rho\left(\overline{u_i' u_k'}\frac{\partial u_j}{\partial x_k} + \overline{u_j' u_k'}\frac{\partial u_i}{\partial x_k}\right) \tag{12}$$

The pressure strain term is

$$\Pi_{ij} = \overline{p\left(\frac{\partial u_i}{\partial x_j} + \frac{\partial u_j}{\partial x_i}\right)} \tag{13}$$

The dissipation term is

$$\varepsilon_{ij} = -2\mu \frac{\partial \overline{u_i'}}{\partial x_k}\frac{\partial \overline{u_i'}}{\partial x_k} \tag{14}$$

where i, j, and k are the vector directions, x, y, and z are Cartesian coordinates, t is time in s, u_i is velocity in m/s, $\overline{u_i}$ is the average velocity component in each coordinate direction in m/s, u_i' is the fluctuating velocity component in the coordinate direction in m/s, g is gravitational acceleration in m/s^2, and p is the pressure in Pa.

3.1.2. Physical Model and Boundary Conditions

Physical models (a) to (f) for six groups of swirlers with different inlet setting angles were generated using the BladeGen 2020 software. The inlet setting angle φ_{in} of swirler (e) is 83°, which was obtained from Equation (4) at the median of blade when R_i = 0.5H. The swirler (f)' φ_{in} increases linearly from 80° to 84° along the blade height from the bottom to top which is shown in Figure 2a, the values of which were calculated by Equation (4). The swirler (a) has a straight blade which is commonly used in dynamic hydrocyclones [17,18,32,33], of which φ_{in} is 0°. The inlet setting angle was divided evenly into four parts from 0° (swirler (a)) to 80° (swirler (f)), which is 20°, 40°, and 60°, and then assigned these values to φ_{in} of the swirlers (b) to (d), respectively. The parameters of the six groups of swirlers are the same, except for the varied inlet setting angles.

A polyhedral mesh was used to mesh the models, and grid refinement was performed for the end and rotating regions of the swirlers. The physical model and grid of the TDH with swirler (f) are shown in Figure 3, where Z = 10 mm and Z = 80 mm correspond to the inlet and outlet sections of the swirler, respectively, while Z = 35 mm and Z = 60 mm are the internal cross-sections of the swirler.

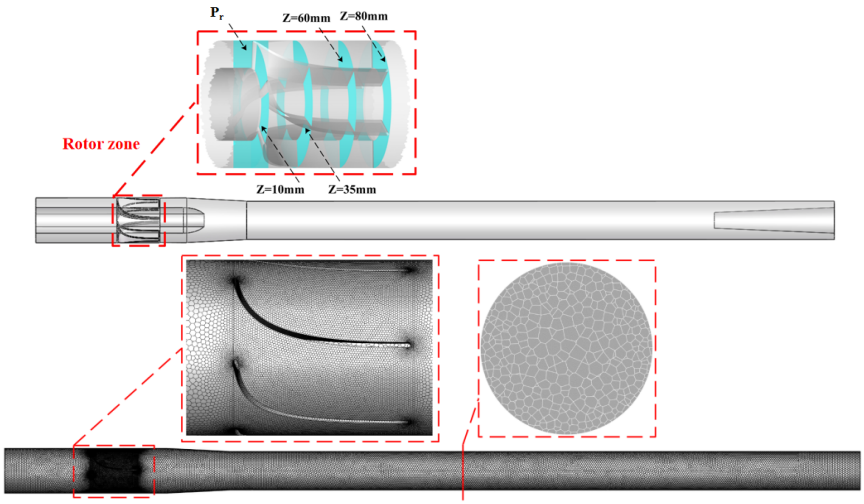

Figure 3. Physical model and grid of the TDH with the LSRS.

Ansys Fluent 2020 was used for the numerical solution. Specifically, the double-precision implicit solution method, steady-state mode, and Eulerian multiphase flow model were used. The pressure–velocity coupled equations were solved using the Semi-Implicit Method for Pressure Linked Equations (SIMPLE) algorithm, in which the pressure calculation equations employed the pressure staggered option (PRESTO!) scheme, and the other equations used the higher-order quadratic upwind interpolation (QUICK) spatial discretization scheme. The rotational swirler was modeled by frame motion (MRF). All walls of the swirler were set as rotating walls, while the other walls were set as non-slip stationary walls. The velocity inlet was used as the inlet boundary condition, and the underflow and overflow were both set as the outflow. The hydraulic residence time of the low-shear tubular dynamic hydrocyclone was 1.7 s, ignoring the effect of temperature, which was set at 20 °C. The continuous phase was set as water, the density and viscosity of which were 998 kg/m^3 and 1.0 mPa·s, respectively. The dispersed phase was set as lubricant 32, the density and viscosity of which were 821 kg/m^3 and 38 mPa·s, respectively.

3.1.3. Grid Independence Verification

Gridding is the most important step in numerical simulation, and the number, quality, and type of grid cells have a significant effect on the accuracy and speed of the simulation. To ensure calculation accuracy and efficiency, four different numbers of grids were tested, and the tangential velocities in the Z = 10 mm cross-section are shown in Figure 4. When

more than 87 × 10^4 grid cells were used, the tangential velocity in the Z = 10 mm section of the TDH was essentially constant, and the calculation results were independent of the grid size.

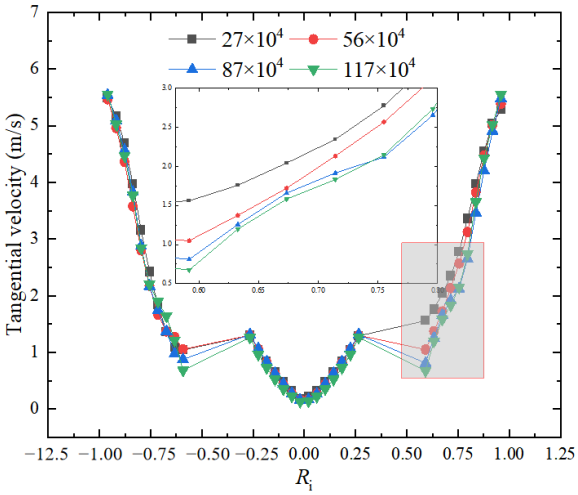

Figure 4. Tangential velocity distribution at Z = 10 mm under different numbers of grids.

3.2. Analysis of Numerical Simulation Results

3.2.1. Velocity Analysis

In TDH, the shearing effect of the rotating swirler on the droplets is usually caused by the rapid change in the tangential velocity near the inlet of the swirler, and the shear stress is given as

$$\overrightarrow{\tau_{\theta z}} = \mu \frac{\partial \overrightarrow{V_{\theta-\mathrm{in}}}}{\partial z} \tag{15}$$

where μ is the viscosity of the continuous fluid in Pa·s and $\overrightarrow{V_{\theta-\mathrm{in}}}$ is the absolute tangential velocity at the inlet section of the swirler in m/s.

The tangential velocity variation on the cross-section of the dynamic hydrocyclones has been studied in all the existing literatures [17,18,32,33], however, little attention has been paid to the variation of the tangential velocity along the axial direction of the hydrocyclone. It can be seen from Equation (15) that a major factor in the oil droplets' breakup is the rapid change along the axial direction of the tangential velocity. A radial plane is created in the zone of Z = 0–20 mm, where liquid flows into the blades, which is shown in Figure 3 as P_r. The flow field located 1 mm near the wall is ignored to avoid the boundary effect. Therefore, the range of the radial plane P_r taking in a radial direction is R = 21–34 mm.

The distribution of the tangential velocity in the radial plane P_r for each swirler is shown in Figure 5. As may be seen in Figure 5, the tangential velocity is smooth along the radial in all the swirlers (a) to (f), and thus, the radial change rate of the tangential velocity has little effect on the particle size of the dispersed phase. The tangential velocity has a drastic fluctuation along the axial direction Z for swirlers (a) to (d), when the fluid flows into the swirler (at the blade inlet of Z = 10 mm). By contrast, in the LSRSs (swirlers (e) and (f)), the axial gradient of the tangential velocity has the smoothest variation in the region away from the blade.

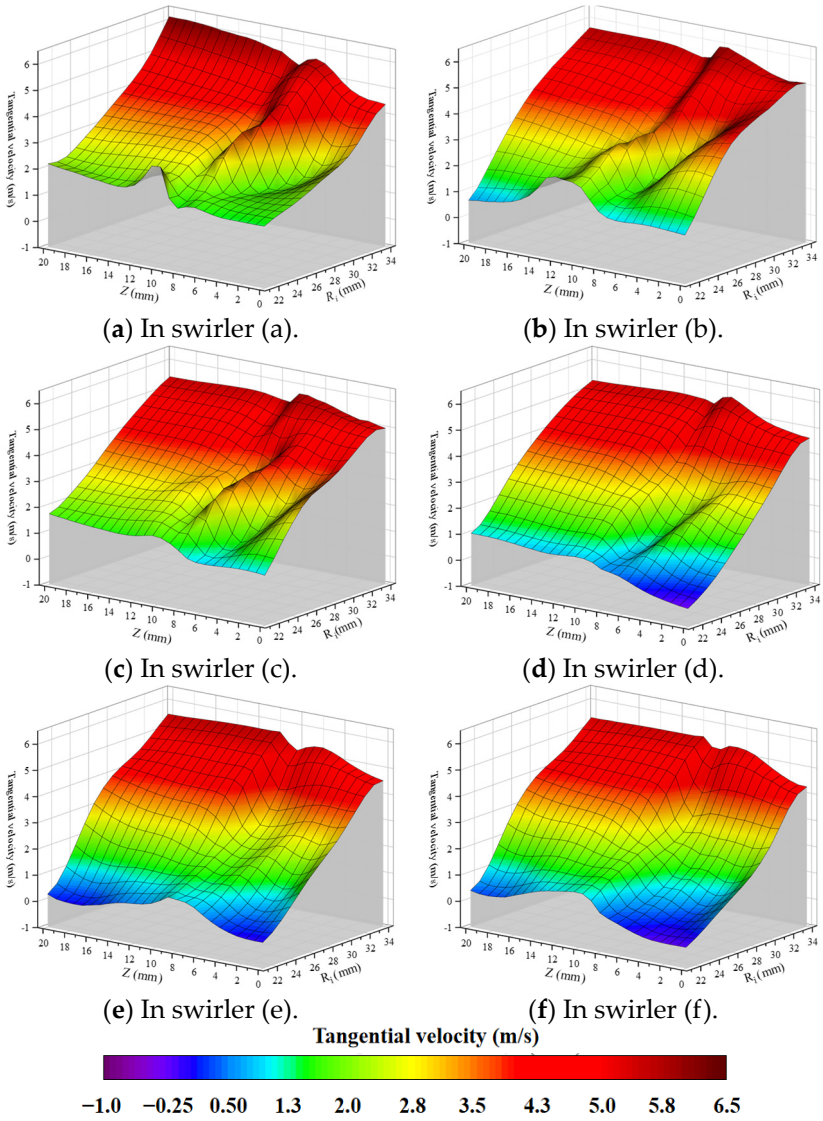

(**a**) In swirler (a). (**b**) In swirler (b).

(**c**) In swirler (c). (**d**) In swirler (d).

(**e**) In swirler (e). (**f**) In swirler (f).

Figure 5. Tangential velocity in the radial plane within the zone of Z = 0–20 mm distribution.

The average value of the maximum shear stress under a cylindrical surface of radius R_i in any swirler is

$$\overline{\tau}_{\max-n-R_i} = \frac{1}{6}\sum_{N=1}^{6} \tau_{\max-n-R_i-N} \tag{16}$$

where $\tau_{\max}$ is the maximum shear stress in Pa; N is the serial number of the flow channel; and n is the serial number of the swirler; specifically, n can be a, b, c, d, e, and f. The $\tau_{\max\text{-}n\text{-}Ri\text{-}N}$, for any swirler at any radial position, is calculated by simulation.

The critical droplet size at which droplets may break up on a cylindrical surface of the radius R_i at the mean maximum shear stress $d_{\text{crit-n-Ri}}$ is

$$d_{\text{crit}-\text{n}-\text{R}_\text{i}} = \frac{4\sigma}{\overline{\tau}_{\max-n-R_i}} \tag{17}$$

where σ is the oil–water interfacial tension in N/m. The σ value was set to 0.029 N/m, which is the interfacial tension between lubricant 32 and water at 20 °C.

The relative critical droplet size values of swirlers (b) to (f), on the same cylindrical surface, are transformed to the dimensionless by being divided by the critical droplet size value of swirlers (a),

$$d_{re-n-R_i} = \frac{d_{\mathrm{crit-n-R_i}} - d_{\mathrm{crit-a-R_i}}}{d_{\mathrm{crit-a-R_i}}} \tag{18}$$

and the global average relative droplet size of swirler is expressed by the dimensionless number $\overline{d}_{re-n}$,

$$\overline{d}_{re-n} = \sum_{R_i=21}^{34} d_{re-n-R_i} \tag{19}$$

The relative critical droplet size value of the swirlers (b) to (f) are computed from Equations (16) to (19) for different cylindrical surfaces, as shown in Figure 6. The R_i in the legend of Figure 6 is the radius of the cylindrical surface. It can be seen that the average relative droplet sizes of swirlers are (e), (d), (b), (f), and (c) in the order of high to low.

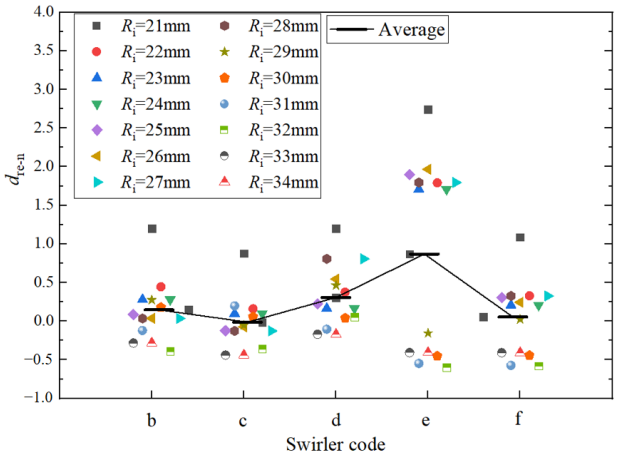

Figure 6. Relative droplet size distribution.

3.2.2. Turbulence Analysis

The turbulence energy dissipation rate is an important parameter for evaluating the strength of turbulence; it also reflects the amount of the turbulence kinetic energy acting on the droplet surfaces through the flow field. Figure 7 shows the turbulence energy dissipation rates of the swirler (a) to swirler (f) in the Z = 10 mm, 35 mm, 60 mm, and 80 mm sections, which are located near the entrance, middle, and exit positions of the swirler and are shown in Figure 3. Overall, the peak turbulence energy dissipation rates appeared at the swirler inlet (Z = 10 mm), where the tangential velocity also has a drastic fluctuation along the axial direction Z.

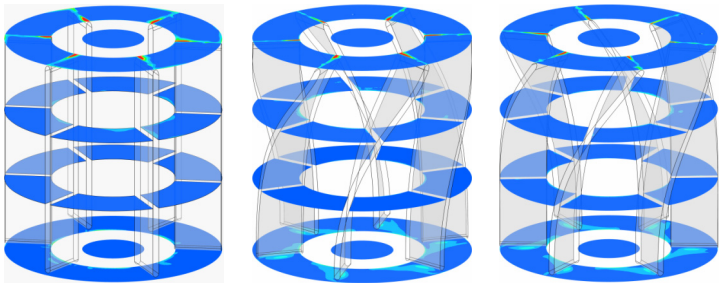

(**a**) In swirler (a). (**b**) In swirler (b). (**c**) In swirler (c).

Figure 7. *Cont.*

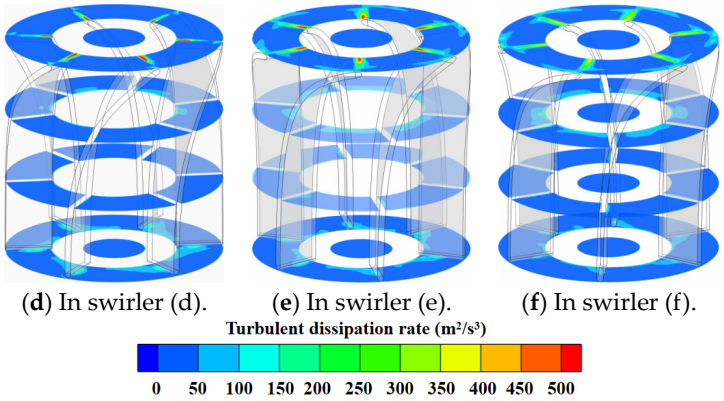

(**d**) In swirler (d). (**e**) In swirler (e). (**f**) In swirler (f).

Figure 7. Turbulence energy dissipation rate in the sections of Z = 10 mm, 35 mm, 60 mm, and 80 mm.

The peak turbulence energy dissipation rate of swirler (a), which has a straight blade, is the maximum at 400 m^2/s^3. The distribution of the turbulence energy dissipation rate in the LSRS (swirler (f)) is more uniform than that of the non-low-shear swirlers. In addition, the peak turbulence energy dissipation rate in all sections of swirler (f) is 60 m^2/s^3, which is less than 1/7 of the peak turbulence energy dissipation rate in swirler (a).

Based on the Kolmogorov–Hinze theory, the maximum stable droplet size d_{95} under the action of turbulence during the swirling process is predicted as

$$d_{95}\left(\frac{\rho_c}{\sigma}\right)^{\frac{3}{5}}\varepsilon^{\frac{2}{5}} = C \tag{20}$$

where C is a constant, ε is the turbulence energy dissipation rate in m^2/s^3, and ρ_c is the density of the continuous phase in kg/m^3.

The maximum turbulence energy dissipation rate occurred in the Z = 10 mm section and the corresponding d_{95} was calculated. The dimensionless numbers $\varepsilon_{re\text{-}max}$ and $d_{re\text{-}max}$ is defined as

$$\varepsilon_{re-max} = \frac{\varepsilon_{max-n} - \varepsilon_{max-a}}{\varepsilon_{max-a}} \tag{21}$$

$$d_{re-max} = \frac{d_{95-n} - d_{95-a}}{d_{95-a}} \tag{22}$$

where $\varepsilon_{max\text{-}a}$ is the maximum turbulence energy dissipation rate of swirler (a), and the subscripts n are the serial numbers of the swirlers.

The differences in the $\varepsilon_{re\text{-}max}$ and $d_{re\text{-}max}$ between the LSRS and the non-low-shear rotating swirlers are highlighted in Figure 8. Compared to the straight swirler (a), LSRS (f) exhibited a 68.5% reduction in $\varepsilon_{re\text{-}max}$, while its $d_{re\text{-}max}$ increased to 0.6 times that of the straight swirler.

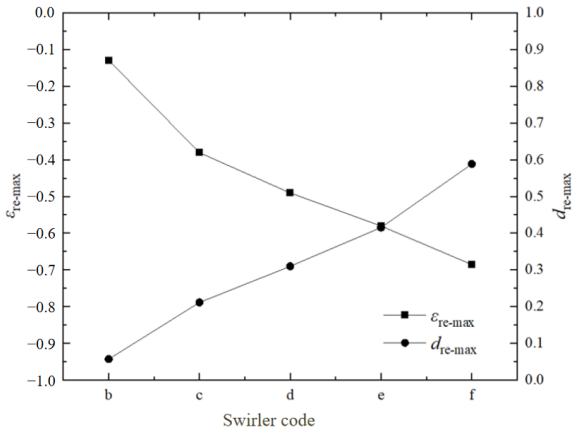

Figure 8. $\varepsilon_{re\text{-}max}$ and $d_{re\text{-}max}$ corresponding to the Z = 10 mm cross-section.

4. Field-Experiment-Based Verification

Based on the LSRS, a prototype of TDH with a capacity of 5 m^3/h was designed and tested on an offshore oil platform of CNOOC Ltd. (Beihai, China). The production process of the oil field is shown in Figure 9a. The liquid produced from the oil well passes through a gas-liquid trap for initial degassing and then through a two-stage tandem three-phase separator for oil-gas-water separation. The separated gas phase is discharged into a natural gas processing module; the oil phase is dewatered to the required standard by the electric dehydrator and discharged into the crude oil buffer tank. The produced water is first transferred to a buffer tank and then cleaned by a static hydrocyclone and a multimedia filter. The cleaned water is then injected back into the ground. During the test, the inlet of the TDH was connected to the rich water outlet of the first stage three-phase separator.

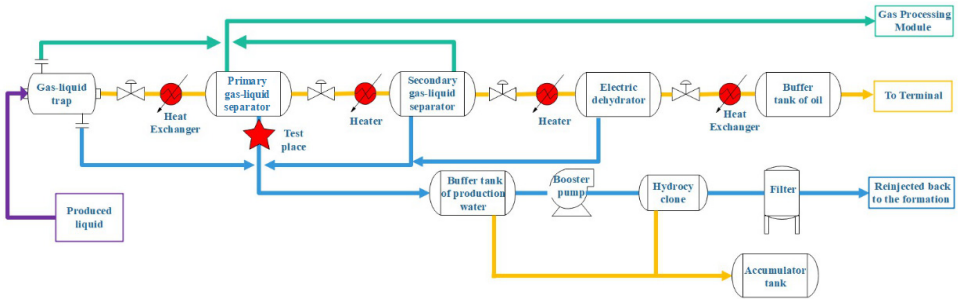

(**a**) Oilfield oil-gas-water processing

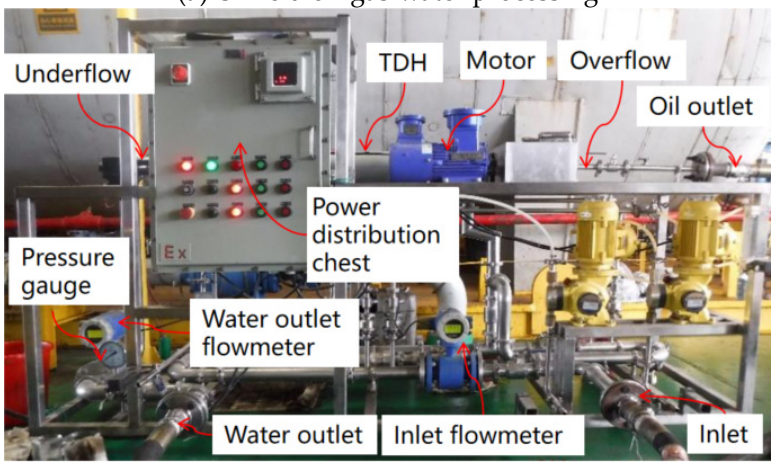

(**b**) Experimental setup

Figure 9. TDH experimental system.

The low-shear TDH used in the field experiment is shown in Figure 9b. The inlet pressure and temperature during the experiment were 0.4 MPa and 64 °C, and the density and viscosity of the dispersed oil phase is 880 kg/m^3 and 30 mPa·s, respectively. The oil concentration at the TDH inlet and underflow was measured by a Spectro Scientific InfraCal 2 oil content meter. Further, n-hexane was employed as the extractant.

The TDH was operated continuously for more than 36 h on the offshore platform, and according to the field experimental results, the equipment showed good separation efficiency under the design conditions. Furthermore, the oil concentration in the underflow was always less than 40 mg/L. To test the separation performance and adaptability of the TDH, the splitting ratio was set as 10%, and the sampling interval was 2 h. The oil concentration and separation efficiency are shown in Figure 10; the average separation efficiency was 83%, which is 20% higher than the on-site static hydrocyclones, and the average oil content in the underflow was 27 mg/L. Notably, the TDH had a good separation efficiency when the fluctuation of the flow rate was within 50%, and the equipment was stable and reliable in continuous operation.

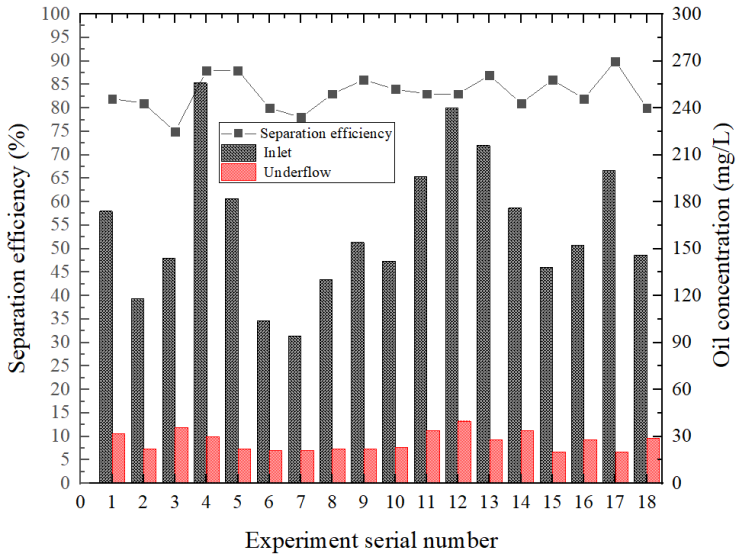

Figure 10. Separation efficiency and oil concentration in the stable operation experiment.

5. Conclusions

A design methodology was proposed for the low-shear rotating swirler (LSRS). The variation of the tangential velocity along the axial and radial direction were studied, and make up for the deficiency of the spatial variation of the tangential velocity in the dynamic cyclone separator. The shear stress and turbulence energy dissipation rate in the rotating swirler with different inlet setting angles were simulated using ANSYS Fluent 2020. The results demonstrated that, compared with the straight-blade rotating swirler, the TDH with LSRS reduced the maximum shear stress by 74.6% and the peak turbulence energy dissipation rate by 68.5%, and increased the maximum stable diameter by 0.6 times compared to that of the straight-bladed rotating swirler. During continuous operation for more than 36 h on an offshore oil platform, the average separation efficiency of the LSRS-equipped TDH was 83%, which is 20% higher than the on-site static hydrocyclones, and the average underflow oil concentration was 27 mg/L.

The LSRS design methodology for TDH can help prevent the oil droplets from breaking up before being isolated and increase TDH's separation efficiency. While the research primarily focuses on the entrance angles of the swirler blades, other parameters such as the lengths of the swirler blade, the number of blades, and so on have yet to receive adequate attention.

Author Contributions: Conceptualization, Y.J., J.C. and X.W.; methodology, Z.S., X.W., H.D., H.Y. and Q.R.; software, H.Y. and Q.R.; formal analysis, H.D. and Q.R.; investigation, Z.H.; data curation, H.Y. and Z.H.; writing—original draft preparation, Z.S.; writing—review and editing, Y.J., J.Z. and Z.H.; validation, J.Z.; project administration, J.C. All authors have read and agreed to the published version of the manuscript.

Funding: This work was supported by the key project supported by the National Natural Science Foundation of China Joint Fund for Enterprise Innovation and Development (No. U20B2030), and the National Natural Science Foundation of China (No.52274059).

Data Availability Statement: No new data were created or analyzed in this study. Data sharing is not applicable to this article.

Conflicts of Interest: The authors declare no conflict of interest.

References

1. Ghafoorim, S.; Omar, M.; Koutahzadeh, N.; Zendehboudi, S.; Malhas, R.N.; Mohamed, M.; Al-Zubaidi, S.; Redha, K.; Baraki, F.; Mehrvar, M. New advancements, challenges, and future needs on treatment of oilfield produced water: A state-of-the-art review. *Sep. Purif. Technol.* **2022**, *289*, 120652. [CrossRef]
2. Hou, D.; Liu, P.; Zhao, Q.; Jiang, L.; Cui, B.; Wei, D. Numerical Study on the Separation Performance of Hydrocyclones with Different Secondary Cylindrical Section Diameters. *Processes* **2023**, *11*, 2542. [CrossRef]
3. Jiang, L.; Liu, P.; Zhang, Y.; Yang, X.; Li, X.; Zhang, Y.; Wang, H. Particle Motion Characteristics in W-Shaped Hydrocyclones. *Separations* **2021**, *8*, 121. [CrossRef]
4. Zhou, N.; Gao, Y.; An, W.; Yang, M. Investigation of velocity field and oil distribution in an oil-water hydrocyclone using a droplet dynamics analyzer. *Chem. Eng. J.* **2010**, *157*, 73–79. [CrossRef]
5. Gong, H.; Yang, Y.; Yu, B.; Luo, X.; Peng, Y.; Jiang, Y. Coalescence characteristics of droplets dispersed in oil subjected to electric and centrifugal fields. *Colloids Surf. A Physicochem. Eng. Asp.* **2022**, *648*, 129398. [CrossRef]
6. Liu, S.; Zhang, D.; Yang, L.; Xu, J. Breakup and coalescence regularity of non-dilute oil drops in a swirler-type swirling flow field. *Chem. Eng. Res. Des.* **2018**, *129*, 35–54. [CrossRef]
7. Liu, S.; Yang, L.; Zhang, D.; Xu, J. Separation characteristics of the gas and liquid phases in a swirler-type swirling flow field. *Int. J. Multiph. Flow* **2018**, *107*, 131–145. [CrossRef]
8. Li, F.; Fu, W.; Liu, P. Investigation of optimal design and separation performance of the hydrocyclone with a vorticose involute-line diversion feeding body. *Powder Technol.* **2022**, *405*, 117523. [CrossRef]
9. Al-Kayiem, H.H.; Hamza, J.E.; Lemmu, T.A. Performance enhancement of axial concurrent liquid–liquid hydrocyclone separator through optimization of the swirler vane angle. *J. Pet. Explor. Prod. Technol.* **2020**, *10*, 2957–2967. [CrossRef]
10. Cai, B.; Wang, J.; Sun, L.; Zhang, N.; Yan, C. Experimental study and numerical optimization on a vane-type separator for bubble separation in TMSR. *Prog. Nucl. Energy* **2014**, *74*, 1–13. [CrossRef]
11. Mao, R.; Li, Y.; Liu, Y.; Zhu, H.; Wang, N.; Yang, Q.; Lu, H. Separation characters of an axial-flow hydrocyclone with oil collecting pipe. *Sep. Purif. Technol.* **2023**, *305*, 122139. [CrossRef]
12. Zeng, X.; Xu, Y.; Zhao, L.; Fan, G.; Yan, C. Numerical investigation on axial liquid-liquid separators with different swirl chambers. *Chem. Eng. Process. Process Intensif.* **2021**, *161*, 108324. [CrossRef]
13. Tian, Y.; He, L.; Luo, X. Numerical simulation of the effect on flow field of two different methods of guide swirlers in liquid-liquid cyclones. *Sci. Technol. Eng.* **2018**, *18*, 153–158. [CrossRef]
14. He, M.; Tian, Y.; Luo, X. A new method for the guide swirlers design in double—Cone liquid—Liquid cyclon. *Acta Pet. Sin. (Pet. Process. Sect.)* **2018**, *34*, 155–165. [CrossRef]
15. Xing, L.; Jiang, M.; Zhang, Y. Design of De-oiling separator based on oil droplets migration trajectory. In *Proceedings of the International Field Exploration and Development Conference 2018*; Springer: Singapore; pp. 1716–1727. [CrossRef]
16. Xing, L.; Li, J.; Jiang, M.; Zhao, L.; Han, G. Flow field analysis and performance evaluation of a hydrocyclone coalescer. *Sep. Sci. Technol.* **2022**, *57*, 3035–3052. [CrossRef]
17. Chen, J.; Hou, J.; Li, G.; Xu, C.; Zheng, B. The Effect of Pressure Parameters of a Novel Dynamic Hydrocyclone on the Separation Efficiency and Split Ratio. *Sep. Sci. Technol.* **2015**, *50*, 781–787. [CrossRef]
18. Huang, L.; Deng, S.; Guan, J.; Chen, M.; Hua, W. Development of a novel high-efficiency dynamic hydrocyclone for oil–water separation. *Chem. Eng. Res. Des.* **2018**, *130*, 266–273. [CrossRef]
19. Jiao, J.; Zheng, Y.; Wang, J.; Sun, G. Experimental and numerical investigations of a dynamic cyclone with a rotary impeller. *Chem. Eng. Process. Process Intensif.* **2008**, *47*, 1861–1866. [CrossRef]
20. Zhang, Z.; Shao, M.; Ling, X. Experimental study on the separation performance of a novel gas–liquid separator. *Adv. Powder Technol.* **2022**, *33*, 103795. [CrossRef]
21. Liu, P.; Ren, Y.; Feng, M.; Wang, D.; Hu, D. A performance analysis of inverse two-stage dynamic cyclone separator. *Powder Technol.* **2019**, *351*, 28–37. [CrossRef]
22. Bella, A.D.; Anthony, M.M. Apparatus with Voraxial Separator and Analyzer. U.S. Patent 6248231B1, 19 June 2001.
23. Richter, H.E. Method and Apparatus for Separating Fluids Having Different Specific Gravities. U.S. Patent 5084189, 21 September 1990.
24. Bella, A.D.; Anthony, M. Voraxial Filtration System with Self-Cleaning Auxiliary Filtration Apparatus. U.S. Patent 7727386B2, 21 November 2003.
25. Perissinotto, R.M.; Verde, W.M.; Perles, C.E.; Biazussi, J.L.; Castro, M.S.; Bannwart, A.C. Experimental analysis on the behavior of water drops dispersed in oil within a centrifugal pump impeller. *Exp. Therm. Fluid Sci.* **2020**, *112*, 109–124. [CrossRef]
26. Perissinotto, R.M.; Verde, W.M.; Castro, M.S.; Biazussi, J.L.; Estevam, V.; Bannwart, A.C. Experimental investigation of oil drops behavior in dispersed oil-water two-phase flow within a centrifugal pump impeller. *Exp. Therm. Fluid Sci.* **2019**, *105*, 11–26. [CrossRef]
27. Perissinotto, R.M.; Verde, W.M.; Gallassi, M.; Goncalves, G.F.N.; Castro, M.S.; Carneiro, J.; Biazussi, J.L.; Bannwart, A.C. Experimental and numerical study of oil drop motion within an ESP impeller. *J. Pet. Sci. Eng.* **2019**, *175*, 881–895. [CrossRef]
28. Cerqueira, R.F.L.; Perissinotto, R.M.; Verde, W.M.; Biazussi, J.L.; Castro, M.S.; Bannwart, A.C. Development and assessment of a particle tracking velocimetry (PTV) measurement technique for the experimental investigation of oil drops behaviour in dispersed oil–water two-phase flow within a centrifugal pump impeller. *Int. J. Multiph. Flow* **2023**, *159*, 104302. [CrossRef]

29. Liu, Y.; Lu, H.; Li, Y.; Xu, H.; Yang, Q. A review of treatment technologies for produced water in offshore oil and gas fields. *Sci. Total Environ.* **2021**, *775*, 145485. [CrossRef]
30. Wu, D.; Xia, F.; Lin, S.; Cai, X.; Zhang, H.; Liu, W.; Li, Y.; Zhang, R.; Zhang, Y.; Zhang, X.; et al. Effects of secondary emulsification of ASP flooding produced fluid during surface processes on its oil/water separation performances. *J. Pet. Sci. Eng.* **2021**, *202*, 108426. [CrossRef]
31. Murthy, Y.R.; Bhaskar, K.U. Parametric CFD studies on hydrocyclone. *Powder Technol.* **2012**, *230*, 36–47. [CrossRef]
32. Long, H.; Deng, S.; Chen, M.; Guan, J. Numerical simulation and experimental study on a deoiling rotary hydrocyclone. *Chem. Eng. Sci.* **2017**, *172*, 107–116. [CrossRef]
33. Galletti, C.; Rum, A.; Turchi, V.; Nicolella, C. Numerical analysis of flow field and particle motion in a dynamic cyclonic selector. *Adv. Powder Technol.* **2020**, *31*, 1264–1273. [CrossRef]